JOURNAL OF SOLID STATE CHEMISTRY **133,** 445–457 (1997)
ARTICLE NO. SC977509

Structural Properties and Oxygen Stoichiometry of $(Pr_{1.5}Ce_{0.5})Sr_2Cu_2TaO_{10-\delta}$ and $(R_{1.5-x}Pr_xCe_{0.5})Sr_2Cu_2NbO_{10-\delta}$, R = Nd, Sm, Eu: Correlations with Electronic and Magnetic Properties

T. J. Goodwin,*,[1] H. B. Radousky,*,† and R. N. Shelton*

*Department of Physics, University of California, Davis, California 95616; and †Lawrence Livermore National Laboratory, Livermore, California 94550

Received August 20, 1996; in revised form June 11, 1997; accepted June 12, 1997

The structural parameters, phase purity, and oxygen stoichiometry of the $(Pr_{1.5}Ce_{0.5})Sr_2Cu_2TaO_{10-\delta}$ and $(R_{1.5-x}Pr_xCe_{0.5})Sr_2Cu_2NbO_{10-\delta}$, R = Nd, Sm, Eu, compounds are investigated with powder X-ray diffraction (XRD), Rietveld refinements, and thermogravimetric analysis (TGA). The XRD data indicate that all the $(R_{1.5-x}Pr_xCe_{0.5})Sr_2Cu_2NbO_{10-\delta}$ compounds are isostructural and typically 98% pure. Rietveld refinements reveal a contraction of the c lattice parameter and features in the rare earth–planar oxygen bond length (as functions of Pr doping) that are correlated with the unusual electronic and magnetic transitions induced by the Pr ion in these materials. Results for deoxygenated samples show that the lattice expands upon deoxygenation and suggest that the oxygen is removed primarily from the SrO layers. TGA results reveal reliable techniques for determining oxygen stoichiometries and deoxygenating these compounds and that these compounds are oxygen deficient with δ's of typically 0.045. The structural features of these compounds are compared to similar high T_C cuprates, and related to the electronic and magnetic transitions and the suppression of superconductivity induced by the Pr ion in these materials. We discuss our results in terms of the current understanding of high T_C cuprates and models for the suppression of superconductivity by the Pr ion in the related $(R_{1-x}Pr_x)Ba_2Cu_3O_7$ system. © 1997 Academic Press

I. INTRODUCTION

Since the discovery of superconductivity above 30 K in the $(La_{2-x}Ba_x)CuO_4$ system (1) and above liquid nitrogen temperatures in $YBa_2Cu_3O_7$ (2), dozens of superconducting cuprate structures and compounds have been discovered with unusually high superconducting transition temperatures (T_C) (3–5). Among these is the $(R_{1.5}Ce_{0.5})Sr_2Cu_2NbO_{10-\delta}$ [$(R_{1.5}Ce_{0.5})$SCNO] structure illustrated in Fig. 1a. This structure was first reported by Rukang Li *et al.* in 1991 along with a cusp in the resistivity of $(Nd_{1.5}Ce_{0.5})$SCNO near 40 K, suggesting that a small fraction of the compound was superconducting (6). Later that year, Cava *et al.* refined the sample preparation procedure to yield bulk superconductivity below 28 K in the $(Nd_{1.5}Ce_{0.5})Sr_2Cu_2MO_{10-\delta}$, M = Nb, Ta, compounds (7). Since then, the $(R_{1.5}Ce_{0.5})$SCNO structure has been reported to form for R = Pr, Nd, Sm, Eu, and Gd, and the isostructural Ta analogs, $(R_{1.5}Ce_{0.5})Sr_2Cu_2TaO_{10-\delta}$ [$(R_{1.5}Ce_{0.5})$SCTO], have been reported to form for R = Pr, Nd, Sm, and Eu (7–12). With the exception of the R = Pr compounds, all of these materials exhibit bulk superconductivity below ~28 K (7–12).

The primary features of the $(R_{1.5}Ce_{0.5})$SCNO structure are (i) CuO_2 square-planar substructures which are universal to all high T_C cuprate structures and are widely believed to be responsible for the unusual transport properties and unusually high T_C's (3–5), (ii) an R_2O_2 fluorite-like rare earth substructure similar to that found in the R_2CuO_4 T′ structure (Fig. 1d) sandwiched between the CuO_2 planes, and (iii) a SrO–NbO_2–SrO trilayered substructure which sandwiches the CuO_2–R_2O_2–CuO_2 structures and is similar to the BaO–NbO_2–BaO trilayer of the $RBa_2Cu_2NbO_8$ (RBCNO) structure (13) (Fig. 1b) and the BaO–CuO–BaO trilayer of the $RBa_2Cu_3O_7$ (RBCO) structure (4) (Fig. 1c). In terms of well-known high T_C cuprate structures, the $(R_{1.5}Ce_{0.5})$SCNO structure can be described as alternating layers of R_2CuO_4 T′ (RCO) (Fig. 1d) and SrO–NbO_2–SrO structures or as an evolution of the $RBa_2Cu_3O_7$ structure in which NbO_2 planes replace the CuO chains, the square-subplanar rare earth layer is replaced by a R_2O_2 fluorite-type layer, Sr replaces Ba, and a glide plane (n-glide) is introduced at the R_2O_2 layer which doubles the c-axis of the unit cell.

More recently, these compounds have attracted attention due to the unusual magnetic and electronic properties of $(Pr_{1.5}Ce_{0.5})$SCNO and $(Pr_{1.5}Ce_{0.5})$SCTO (8, 14–16). Pr has been found to inhibit superconductivity in these compounds in conjunction with an unexpected insulating electronic state, anomalous Pr magnetism, and a pseudotriplet Pr 4f

[1]To whom correspondence should be addressed.

0022-4596/97 $25.00

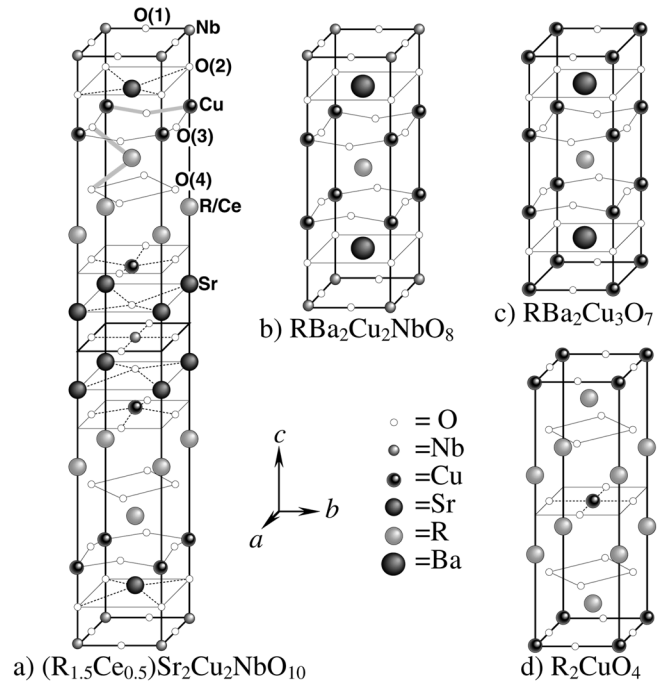

FIG. 1. Unit cells for the (a) $(R_{1.5}Ce_{0.5})Sr_2Cu_2NbO_{10-\delta}$, (b) $RBa_2Cu_2NbO_8$, (c) $RBa_2Cu_3O_7$, and (d) R_2CuO_4 T′ higher T_C cuprate structures. Both the rare earth–nearest neighbor oxygen and intra-CuO_2 planar copper–oxygen bonds are highlighted for the $(R_{1.5}Ce_{0.5})Sr_2Cu_2NbO_{10-\delta}$ structure.

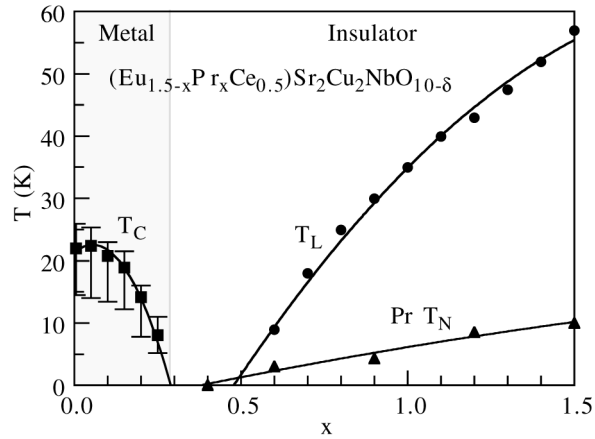

FIG. 2. Phase diagram for the $(Eu_{1.5-x}Pr_xCe_{0.5})Sr_2Cu_2NbO_{10-\delta}$ system taken from Refs. 15 and 22. For $x = 0$, $(Eu_{1.5}Ce_{0.5})Sr_2Cu_2NbO_{10-\delta}$ is metallic and superconducting with $T_C \approx 24$ K. As pr is doped in, T_C (■) is suppressed until $x \approx 0.28$ where the superconductivity is completely suppressed and the system undergoes a metal-to-insulator transition. For $0.3 \leq x < 1.5$, the system is electronically insulating. For $x > 0.6$, the system exhibits Pr magnetism below T_N (▲) and a Cu spin reorientation at T_L (●). The T_C's were determined from the midpoint of the superconducting transition in the magnetic data: error bars on the plot represent the 10% and 90% superconducting transition points in the magnetic data (15, 22). The T_N's were determined from the magnetic peak in specific heat data (15, 22). The T_L's were determined from the magnetic signature of the reorientation—a cusp in the magnetic data.

crystal field ground state while all other members of the $(R_{1.5}Ce_{0.5})$SCNO structure are metallic and superconducting (8, 15, 16). Examination of the magnetic and electronic properties of the $(R_{1.5-x}Pr_xCe_{0.5})$SCNO, R = Nd, Sm, Eu, series of compounds indicate that Pr suppresses superconductivity in the $(R_{1.5}Ce_{0.5})$SCNO structure in the same manner as in the RBCO structure (16, 17, 22). The phase diagram for the $(Eu_{1.5-x}Pr_xCe_{0.5})$SCNO system in Fig. 2 illustrates this result. The superconducting transition temperature T_C is suppressed with Pr doping, and at a critical Pr doping level, $x_{cr} \approx 0.28$, superconductivity is completely suppressed in conjunction with a metal-to-insulator transition. Above $x \sim 0.6$, anomalous Pr magnetism appears and develops into the 10 K Pr T_N for $(Pr_{1.5}Ce_{0.5})$SCNO. Also, at $x \approx 0.6$, a reorientation of the ordered Cu spins appears at low temperature (T_L) and develops into the $\sim$57 K Cu spin reorientation found in $(Pr_{1.5}Ce_{0.5})$SCNO (15, 16, 22). The phase diagrams for the $(Sm_{1.5-x}Pr_xCe_{0.5})$SCNO and $(Nd_{1.5-x}Pr_xCe_{0.5})$SCNO systems are nearly identical except that x_{cr} shows an ion size effect: $x_{cr} \approx 0.25$ for $(Sm_{1.5-x}Pr_xCe_{0.5})$SCNO and ≈ 0.22 for $(Nd_{1.5-x}Pr_xCe_{0.5})$SCNO (15, 16, 22). Analysis of the properties of these systems indicate that conventional magnetic pair-breaking or band-filling mechanisms do not adequately explain the suppression of T_C (15–17, 22). We also mention that $(Pr_{1.5}Ce_{0.5})$SCNO shows complex Cu magnetism marked by anitiferromagnetic (AF) order below $\sim$200 K, collinear and noncollinear spin structures, weak ferromagnetic behavior (WF) below $\sim$130 K similar to that found in some RCO compounds [14–16, 18–21], and an interplanar reordering of the Cu spins at $\sim$57 K (T_L in Fig. 2); $(Pr_{1.5}Ce_{0.5})$SCTO shows similar Pr and Cu magnetisms (15, 16, 22). It is evident that the properties of $(Pr_{1.5}Ce_{0.5})$SCNO are representative for high T_C cuprates in terms of crystal structure, anomalous Pr effects, and Cu magnetism. It follows that the issues and controversies surrounding the properties and mechanisms of PrBCO and the RCO T′ compounds are extended to $(Pr_{1.5}Ce_{0.5})$SCNO and $(Pr_{1.5}Ce_{0.5})$SCTO (15, 16). Therefore, studying the $(R_{1.5}Ce_{0.5})$SCNO materials is important for developing our understanding of high T_C cuprates.

We have undertaken an extensive study of the effects of the Pr ion on the properties of the $(R_{1.5}Ce_{0.5})$SCNO family of compounds (8, 15, 16, 22). In this paper we report on our investigations of the phase purity, structural parameters, and oxygen stoichiometry of $(Pr_{1.5}Ce_{0.5})$SCTO and the $(R_{1.5-x}Pr_xCe_{0.5})$SCNO system for R = Nd, Sm, Eu, using X-ray diffraction (XRD), Rietveld refinements of the XRD data, and thermogravimetric analysis (TGA). The structural features of these compounds are compared to similar high

T_C cuprates and related to the electronic and magnetic transitions and the suppression of superconductivity induced by the Pr ion in these materials. We discuss our results in terms of the current understanding of high T_C cuprates and the modeling being developed for the suppression of superconductivity by the Pr ion in the related $(R_{1-x}Pr_x)Ba_2Cu_3O_7$ system.

II. EXPERIMENTAL

Samples of $(Pr_{1.5}Ce_{0.5})$SCTO, $(Eu_{1.5-x}Pr_xCe_{0.5})$SCNO for $0 \le x \le 1.5$, $(Sm_{1.5-x}Pr_xCe_{0.5})$SCNO for $0 \le x \le 1.5$, and $(Nd_{1.5-x}Pr_xCe_{0.5})$SCNO for $0 \le x \le 0.3$ were prepared by standard solid state reaction techniques. Stoichiometric amounts of 99.99% pure or better CeO_2, Pr_6O_{11}, Sm_2O_3, Eu_2O_3, $SrCO_3$, CuO, Nb_2O_5, and Ta_2O_5 were weighed out and ground together using a methanol slurry method in an agate mortar and pestle. The mixed precursors were pressed into 3/4 inch pellets, placed in alumina boats, and fired at 1110°C for 60 h in a tube furnace with ~1.3 atm oxygen pressure flowing at 200 cc/min. The samples were then furance-cooled, reground for 30 min to a fine powder with a mechanized agate mortar and pestle, pressed into $\frac{1}{4}$ inch and $\frac{1}{2}$ inch pellets, and fired as before. Portions of some samples were deoxygenated by grinding them into fine powders and firing at 750°C in a 100 cc/min flowing argon gas atmosphere for 48 h (as prescribed by the TGA results below).

Polycrystalline samples of $Ce_2(Eu_{2-y}Pr_y)O_{(7+y/2)}$ (y = 0.0, 0.5, 1.0, 2.0), $Sr_2(Eu_{1-z}Pr_z)NbO_6$ (z = 0.0, 0.25, 0.5, 1.0), Sr_2PrTaO_6, and $Sr(Nb_{0.67}Cu_{0.33})O_3$, which were used for XRD and oxygen stoichiometry analysis, were prepared by mixing appropriate amounts of 99.99% pure or better CeO_2, Pr_6O_{11}, Eu_2O_3, $SrCO_3$, Nb_2O_5, and Ta_2O_5 with a methanol slurry method in an agate mortar and pestle. These samples were pressed into $\frac{1}{4}$ inch diameter pellets, placed in alumina boats, and fired in air in a box furnace at 1200°C for 12 h and then at 1400°C for 6 h. The samples were then allowed to furnace-cool back to room temperature.

XRD patterns were measured with a Siemens D500 powder X-ray diffractometer equipped with a graphite monochromator. The data were collected over the 2θ range of 10° to 120° at room temperature using Cu$K\alpha$ radiation, a step size of 0.02°, and an 8 s scan time per step. The XRD data were refined to the $I4/mmm$ space group reported for the $(R_{1.5}Ce_{0.5})$SCNO structure (6) over a 2θ range of 20° to 120° using the GSAS software package (23). All atomic site occupancy fractions were fixed (not refined), and only isotropic thermal parameters were used as refinements proved otherwise difficult for this complex structure. Atomic positions and thermal parameters of the Ce and other rare earth ions of any one sample were constrained to the same values since they occupy the same crystallographic position. The final refinements refined 56 parameters over a total of 4998 raw data points representing 140 reflections. Attempts to include impurity phases in the refinements were generally unsuccessful because the additional free parameters and low intensity of the impurity peaks destabilized the refinements.

Thermogravimetric analyses (TGA) were performed with a DuPont 951 TGA using Pt sample boats and atmospheres of air, forming gas (6% H_2/94%N_2), oxygen, or argon flowing at 50 cc/min. The heating sequence used raised the sample temperature at a rate of 5°C/min to 900°C, dwelled for 5 h, then cooled back to room temperature at a rate of 10°C/min. The resolution of the DuPont 951 TGA within normal operational parameters was found to be $\pm$ 0.05 in terms of the oxygen stoichiometry for the $(R_{1.5}Ce_{0.5})$SCNO compounds. This level of uncertainty is unacceptable as typical δ's for the $(R_{1.5}Ce_{0.5})$SCNO compound are about 0.045. Consequently, once the reduction/oxidation chemistry of the compounds was understood and the equilibrium phases of the process were established, samples were similarly reduced or oxidized in a tube furnace in Pt boats under the same flowing atmospheres so that greater accuracy of the initial and final masses could be attained. Initial and final masses of gram size samples could be determined to within 10 μg, giving a theoretical resolution of about 0.001% or an uncertainty of $\pm$0.001 (typically $\pm$0.002 in practice) in terms of oxygen stoichiometry for the $(R_{1.5}Ce_{0.5})$SCNO compounds. This second reduction/oxidation analysis technique will be referred to as high resolution reduction/oxidation analysis or HRROA. Unless otherwise noted, the heating sequence used for HRROA is 20°C/min to 900°C, dwell for 8 h, then furnace-cool back to room temperature. The heating sequence used for our HRROA is different from that of the TGA due to differences in the apparatus used. However, this does not impact our results since we are interested only in the equilibrium phases at the point of our HRROA.

III. RESULTS

A. X-Ray Diffraction and Phase Purity

XRD data show the $(Pr_{1.5}Ce_{0.5})$SCTO and $(R_{1.5-x}Pr_xCe_{0.5})$SCNO, R = Nd, Sm, Eu, samples to possess the tetragonal $I4/mmm$ structure previously reported for the $(R_{1.5}Ce_{0.5})$SCNO compounds (6). The data for most samples showed several weak peaks not associated with the $(R_{1.5}Ce_{0.5})$SCNO structure which we were able to assign to trace amounts of $RSr_2Cu_2NbO_8$, Sr_2RNbO_6, and/or $Sr(Nb_{0.67}Cu_{0.33})O_3$ impurities, where R = Pr, Nd, Sm, and/or Eu (Fig. 3); similar impurities were found for the $(Pr_{1.5}Ce_{0.5})$SCTO sample. Identification of these impurities was difficult since most of their XRD lines are superimposed upon those of the $(R_{1.5}Ce_{0.5})$SCNO structure. However, these impurities were easily identified by extrapolation of non-$(R_{1.5}Ce_{0.5})$SCNO peaks in samples of poorer quality

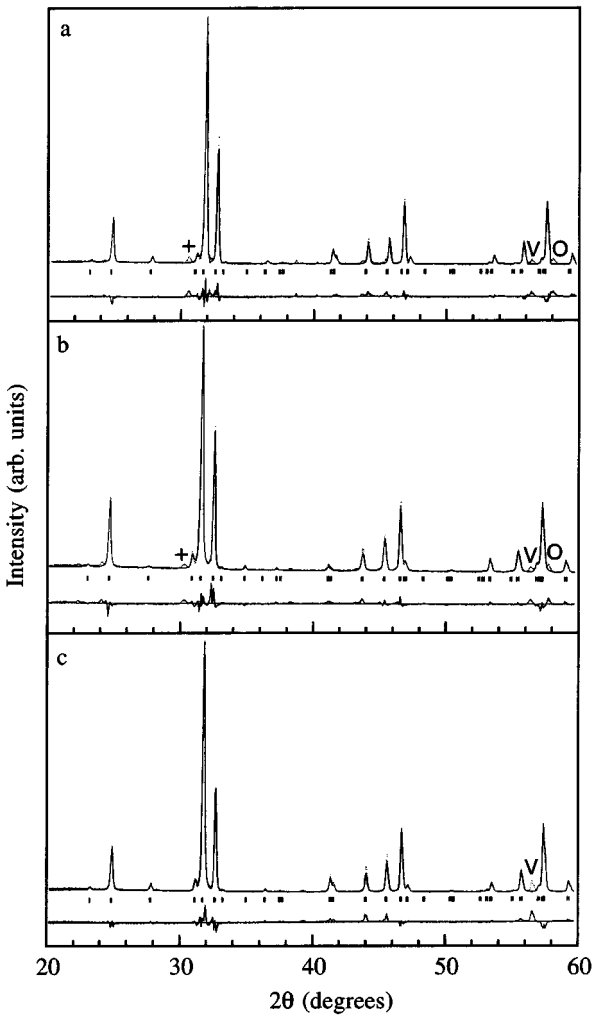

FIG. 3. Rietveld refinements for (a) $(Eu_{1.5}Ce_{0.5})Sr_2Cu_2NbO_{10-\delta}$, (b) $Eu_{0.9}Pr_{0.6}Ce_{0.5})Sr_2Cu_2NbO_{10-\delta}$, and (c) $(Pr_{1.5}Ce_{0.5})Sr_2Cu_2NbO_{10-\delta}$. The plots show only the $20 \leq 2\theta \leq 60$ degree range of the refinements since details above 60 degrees were insignificant on the scale used. Markers indicate the (2 1 3) + (1 1 6) aggregate line of $RSr_2Cu_2NbO_8$ (○), the (1 1 2) + (2 0 0) aggregate line Sr_2RNbO_6 (+), and the (2 1 1) line of $Sr(Nb_{0.67}Cu_{0.33})O_3$ (\/) impurity phases.

(which were not used in this work), where the impurities showed more intense and multiple peaks. In addition, monitoring the relative intensity of these weak peaks as small amounts of the impurities were added to portions of a few samples verified their origin. With the $(R_{1.5}Ce_{0.5})$SCNO phase and these three impurities, we were able to account for all the peaks in the XRD patterns of our samples.

$Sr(Nb_{0.67}Cu_{0.33})O_3$ is a perovskite-type compound which has been reported as an intergrowth phase in $(Nd_{1.5}Ce_{0.5})$SCNO (25) and as a bulk impurity in the related $RSr_2Cu_2NbO_8$ compounds (24). The (2 1 1) and (3 1 0) lines of $Sr(Nb_{0.67}Cu_{0.33})O_3$ could be discerned from close inspection of the XRD data for most samples, the (2 1 1) line being the strongest and most evident (Fig. 3). A $Sr(Ta_{0.67}Cu_{0.33})O_3$ impurity was also detected for $(Pr_{1.5}Ce_{0.5})$SCTO.

Sr_2RNbO_6 are perovskite-type compounds with positional ordering of the R and Nb ions and a monoclinic structural distortion (25). XRD lines from these materials were observed in most of the XRD data of the $(R_{1.5}Ce_{0.5})$SCNO samples and are the strongest lines of those attributed to impurities (Fig. 3). The only lines from this structure clearly observable in the XRD data of our samples are the (1 1 2), (2 0 0), and (less frequently) (3 1 2) lines of the tetragonal unit cell. No peaks from Sr_2PrTaO_6 were observed for the $(Pr_{1.5}Ce_{0.5})$SCTO sample.

$NdSr_2Cu_2NbO_8$ has been reported as a defect structure in $(Nd_{1.5}Ce_{0.5})$SCNO (26) and our results indicate that the $RSr_2Cu_2NbO_8$ phase occurs as a bulk impurity/defect structure for all of the $(R_{1.5}Ce_{0.5})$SCNO compounds. Only a single $RSr_2Cu_2NbO_8$ line was observed in some samples' XRD data, which was the aggregate (2 1 3) + (1 1 6) line situated between the $(R_{1.5}Ce_{0.5})$SCNO (2 1 7) and (1 0 17) lines (Figs. 3 and 4b). The intensity of the (2 1 3) + (1 1 6) line makes it the only prominent line of the $RSr_2Cu_2NbO_8$ structure that appears in the XRD data which does not coincide with lines of the $(R_{1.5}Ce_{0.5})$SCNO structure. No peaks from $PrSr_2Cu_2TaO_8$ could be detected in the XRD data for the $(Pr_{1.5}Ce_{0.5})$SCTO sample.

XRD analysis similar to that used by Bennahmias *et al.* (27) to determine the $PrBaO_3$ impurity level in $PrBa_2Cu_2NbO_8$ was used to determine the sensitivity of our XRD method to impurity levels and quantify the phase purity of the $(R_{1.5}Ce_{0.5})$SCNO samples. Mixtures of $(Pr_{1.5}Ce_{0.5})$SCNO plus 0.0, 1.0, and 3.0 formula unit percent (fu%) Sr_2PrNbO_6 were prepared, and XRD data were collected. Results (normalized to the (1 0 7) line of $(Pr_{1.5}Ce_{0.5})$SCNO) are illustrated in Fig. 4a; the (1 1 2) and (2 0 0) lines of Sr_2PrNbO_6 were used in the analysis since they are the strongest Sr_2PrNbO_6 lines. The 0.0 fu% mixture shows no detectable Sr_2PrNbO_6 lines. However, the 1.0 fu% and 3.0 fu% mixtures clearly show the (1 1 2) and (2 0 0) lines of Sr_2PrNbO_6 and that the peak intensities increase with the amount of Sr_2PrNbO_6. Hence, our XRD measurement technique is sensitive to Sr_2PrNbO_6 impurity levels of ~1.0 fu%. The same technique applied to Sr_2EuNbO_6/$(Eu_{1.5}Ce_{0.5})$SCNO, $Sr_2(Cu_{0.33}Nb_{0.67})O_3$/$(Pr_{1.5}Ce_{0.5})$SCNO, $EuSr_2Cu_2NbO_8$/$(Eu_{1.5}Ce_{0.5})$SCNO, and $PrSr_2Cu_2NbO_8$/$(Pr_{1.5}Ce_{0.5})$SCNO mixtures (illustrated in Fig. 4b for the latter mixture) gave similar results. These results allow us to conclude that our $(R_{1.5}Ce_{0.5})$SCNO and $(Pr_{1.5}Ce_{0.5})$SCTO samples are about 98 fu% pure.

XRD data for the deoxygenated $(R_{1.5-x}Pr_xCe_{0.5})$SCNO and $(Pr_{1.5}Ce_{0.5})$SCTO samples showed that, while they retained the $I4/mmm$ $(R_{1.5}Ce_{0.5})$SCNO structure, the lines attributed to the $(R_{1.5}Ce_{0.5})$SCNO phase shifted in a

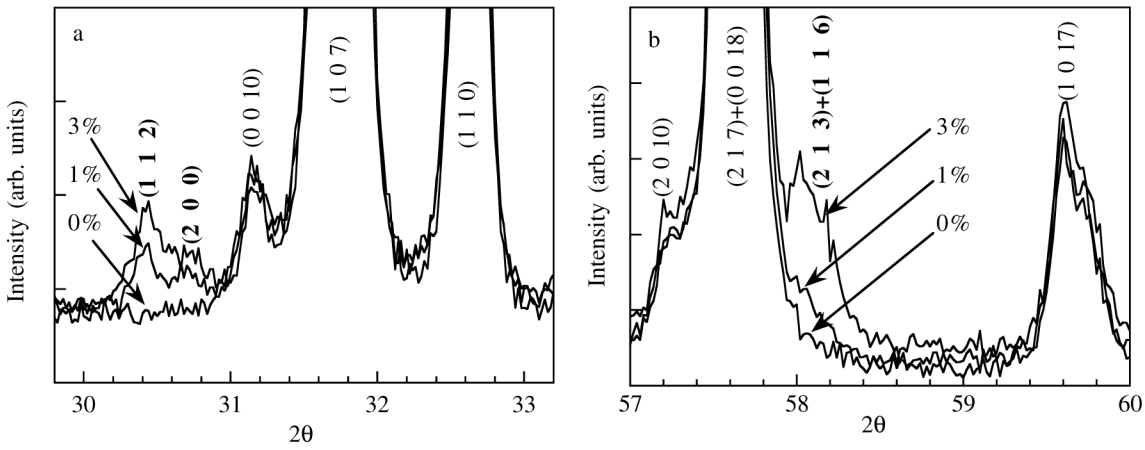

FIG. 4. (a) XRD data for mixtures of $(Pr_{1.5}Ce_{0.5})Sr_2Cu_2NbO_{10-\delta}$ + 0, 1, and 3 fu% Sr_2PrNbO_6. The data show the relative intensities of the (1 1 2) and (2 0 0) lines of Sr_2PrNbO_6 (annotated in bold numbers) with the (0 0 10), (1 1 0), and (1 0 7) lines of $(Pr_{1.5}Ce_{0.5})Sr_2Cu_2NbO_{10-\delta}$; the data of each XRD pattern were normalized to the (1 0 7) line of $(Pr_{1.5}Ce_{0.5})Sr_2Cu_2NbO_{10-\delta}$. (b) XRD data for mixtures of $(Pr_{1.5}Ce_{0.5})Sr_2Cu_2NbO_{10-\delta}$ + 0, 1, and 3 fu% $PrSr_2Cu_2NbO_8$. The data show the relative intensities of the aggregate (2 1 3) + (1 1 6) line of $PrSr_2Cu_2NbO_8$ (annotated in bold numbers) with the (2 0 10), (2 1 7) + (0 0 18), and (1 0 17) lines of $(Pr_{1.5}Ce_{0.5})Sr_2Cu_2NbO_{10-\delta}$; the data of each XRD pattern were normalized to the (2 1 7) + (0 0 18) lines of $(Pr_{1.5}Ce_{0.5})Sr_2Cu_2NbO_{10-\delta}$.

manner consistent with an expansion of the lattice. This result is not surprising since removal of oxygen from the lattice is expected to weaken the crystal binding and result in an expansion of the lattice. Analysis of the sample phase purity after deoxygenation showed no detectable change in sample purity.

XRD patterns of the Sr_2PrNbO_6, Sr_2PrTaO_6, and Sr_2EuNbO_6 samples show that the structures and lattice parameters match those previously reported for these compounds (24) and that they are phase pure to within the resolution of our XRD measurement technique. XRD patterns of $Sr_2(Pr_{0.5}Eu_{0.5})NbO_6$ and $Sr_2(Pr_{0.25}Eu_{0.75})NbO_6$ indicate that these compounds possess distorted perovskite-type structures similar to Sr_2PrNbO_6 and Sr_2EuNbO_6, are phase pure, and have lattice parameters intermediate between those of Sr_2PrNbO_6 and Sr_2EuNbO_6.

XRD data showed $Ce_2Eu_2O_7$ to possess the expected fluorite-related M_2O_3 structure and lattice parameters for $Ce_2Eu_2O_7$ (28) and to be phase pure. The XRD data for $Ce_2Pr_2O_8$ showed it to possess the CeO_2 fluorite structure with a lattice parameter of 0.5391 nm, which is less than the reported 0.5402 nm for $Ce_2Pr_2O_7$ (29) and consistent with a contraction of the lattice due to oxidation of the Pr^{3+} ion to the smaller Pr^{4+} ion. XRD data of $Ce_2(Eu_{1.5}Pr_{0.5})O_{7.25}$ and $Ce_2(EuPr)O_{7.5}$ show these compounds to possess a fluorite structure, to have lattice parameters intermediate to those of $Ce_2Eu_2O_7$ and $Ce_2Pr_2O_8$, and to be phase pure to within the resolution of the XRD technique. No superstructure lines could be detected in any of the Ce–R oxide's XRD data, indicating that there is no positional ordering of the rare earths in these compounds.

B. Rietveld Refinements

Figure 3 shows representative Rietveld refinements of the XRD data for $(Pr_{1.5}Ce_{0.5})$SCTO and the $(R_{1.5-x}Pr_xCe_{0.5})$SCNO, R = Nd, Sm, Eu, samples. The goodness-of-fit values (in terms of the reduced chi-square, χ^2, of the fit) for all refinements were between 4% and 6%, and residuals were between 6% and 9% for R, and 9% and 14% for wR_p. Table 1 summarizes the results of the refinements in terms of lattice parameters. Lattice parameters for the $(R_{1.5}Ce_{0.5})$SCNO, R = Pr, Nd, Sm, and Eu, and in agreement with previously reported values (6–12). The lattice parameters for $(Pr_{1.5}Ce_{0.5})$SCTO were larger than for $(Pr_{1.5}Ce_{0.5})$SCNO, consistent with an expected expansion of the lattice due to the replacement of the Nb^{5+} ion with the larger Ta^{5+} ion. Figure 5 shows a plot of lattice parameters and until cell volumes (V_{cell}) for the $(Eu_{1.5-x}Pr_xCe_{0.5})$SCNO and $(Sm_{1.5-x}Pr_xCe_{0.5})$SCNO series determined from the Rietveld analysis. The a lattice parameter increases linearly with increased Pr content. However, the c lattice parameter decreases linearly as Pr is doped from $x = 0.0$ to $x \approx 0.3$. At $x \approx 0.3$, the slope of $c(x)$ begins to change, and at $x \approx 0.6$, $c(x)$ reaches a minimum and then increases to its final value for $(Pr_{1.5}Ce_{0.5})$SCNO and $x = 1.5$. The behavior of the c lattice parameter is reflected in the V_{cell}'s for both series of compounds. The V_{cell}'s curves remain constant for $0.0 < x < 0.3$ and then curve upward for $x > 0.3$. For $x > 0.6$, the $V_{cell}(x)$ curves increases linearly. A contraction of the c lattice parameter is also evident in the data for the $(Nd_{1.5-x}Pr_xCe_{0.5})$SCNO compounds (see Table 1), although the data for this series are incomplete since only

TABLE 1
Representative Lattice Parameters (from Refinements) for the $(Pr_{1.5}Ce_{0.5})Sr_2Cu_2TaO_{10-\delta}$ and $(R_{1.5-x}Pr_xCe_{0.5})Sr_2Cu_2NbO_{10-\delta}$, R = Nd, Sm, Eu, Compounds

x	a (nm)	c (nm)	δ
	$(Eu_{1.5-x}Pr_xCe_{0.5})Sr_2Cu_2NbO_{10-\delta}$		
0.00	0.386631(6)	2.87558(7)	0.048(2)
0.05	0.38666(1)	2.8751(1)	0.044(2)
0.10	0.386689(8)	2.87404(8)	0.048(2)
0.15	0.38670(1)	2.8731(1)	0.044(2)
0.20	0.38689(2)	2.8720(1)	0.045(2)
0.25	0.38681(2)	2.8714(2)	0.041(2)
0.30	0.38689(1)	2.8704(1)	0.049(2)
0.40	0.38705(2)	2.8696(1)	0.043(2)
0.50	0.38720(1)	2.8693(1)	0.040(2)
0.60	0.38736(2)	2.8688(1)	0.043(3)
0.70	0.38750(2)	2.8694(1)	0.041(3)
0.80	0.387610(7)	2.86958(7)	0.044(3)
0.90	0.38779(1)	2.8703(1)	0.043(3)
1.00	0.38797(2)	2.8705(3)	0.050(3)
1.10	0.38808(1)	2.8719(1)	0.043(3)
1.20	0.388226(7)	2.872864(8)	0.044(4)
1.30	0.38838(1)	2.8740(1)	0.042(4)
1.40	0.388551(6)	2.87513(7)	0.049(4)
1.50	0.388739(7)	2.87615(7)	0.048(4)
	Deoxygenated $(Eu_{1.5-x}Pr_xCe_{0.5})Sr_2Cu_2NbO_{10-\delta}$		
d-0.00	0.387010(8)	2.87859(8)	0.148(2)
d-0.60	0.38777(3)	2.8732(3)	0.157(3)
d-0.90	0.38833(2)	2.8779(3)	0.146(3)
d-1.50	0.38924(2)	2.8846(1)	0.163(4)
	$(Sm_{1.5-x}Pr_xCe_{0.5})Sr_2Cu_2NbO_{10-\delta}$		
0.00	0.38713(1)	2.8784(1)	0.042(2)
0.10	0.38705(2)	2.8766(3)	0.042(2)
0.20	0.38720(2)	2.8755(2)	0.038(2)
0.25	0.38725(1)	2.8745(1)	0.040(2)
0.30	0.38729(2)	2.8737(2)	0.044(2)
0.60	0.38766(2)	2.8714(3)	0.040(3)
1.10	0.38821(2)	2.8731(2)	0.042(3)
	$(Nd_{1.5-x}Pr_xCe_{0.5})Sr_2Cu_2NbO_{10-\delta}$		
0.00	0.38822(2)	2.8842(2)	0.037(2)
0.10	0.38818(2)	2.8823(2)	0.039(2)
0.20	0.38830(3)	2.8808(3)	0.040(2)
0.25	0.38837(4)	2.8800(3)	0.037(2)
	$(Pr_{1.5}Ce_{0.5})Sr_2Cu_2TaO_{10-\delta}$		
0.00	0.388512(8)	2.88442(8)	0.049(4)
d-0.00	0.038899(1)	2.8909(2)	0.116(4)

Note. Deoxygenated compounds are indicated with a *d* prefix for *x*.

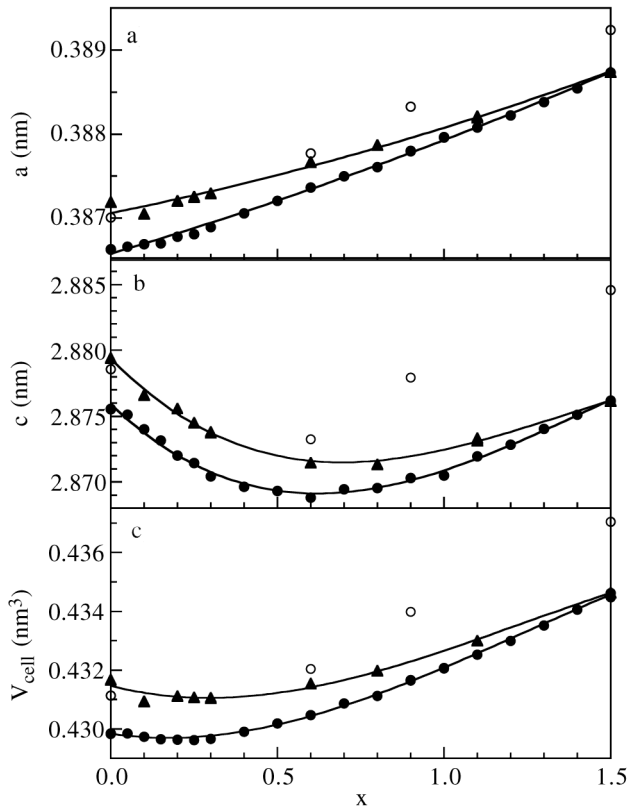

FIG. 5. (a) a lattice parameters, (b) c lattice parameters, and (c) unit cell volumes V_{cell}'s for the $(R_{1.5-x}Pr_xCe_{0.5})Sr_2Cu_2NbO_{10-\delta}$, R = Sm (▲), Eu (●), and deoxygenated R = Eu (○), series of compounds determined from Rietveld refinements of XRD data. The lines serve only as a guide to the eye.

samples for $0.0 \leq x \leq 0.25$ were synthesized. We also mention that the refinement results consistently showed unphysically large thermal parameters for the O(1) crystallographic oxygen sites in the NbO_2 planes (Fig. 1a) for all samples. We interpret this as evidence that the rotation distortion of the Nb–O octahedra reported for $(Nd_{1.5}Ce_{0.5})$ SCNO (26) is also present in all these materials. No other unreasonable thermal parameters were observed for any of the other atomic sites in these compounds.

The structure of the CuO_2 planes is a matter of interest in all high T_C cuprates since it is widely held that these planes are responsible for electronic transport and the unusually large T_C's for these materials. The intraplanar copper–oxygen bond distances Cu–O(3) and bond angles Cu–O(3)–Cu for the $(Eu_{1.5-x}Pr_xCe_{0.5})$SCNO and $(Sm_{1.5-x}Pr_xCe_{0.5})$ SCNO series of compounds determined from refined atomic positions are shown in Fig. 6. The Cu–O(3) bond distances (Fig. 6a) fall between 0.1933 and 0.1945 nm, smaller than 0.1936 and 0.1960 nm for YBCO (30), 0.1950 and 0.1982 nm for PrBCO (30), 0.198 nm for Pr_2CuO_4 (31). The Cu–O(3)–Cu bond angles (Fig. 6b) are between 170° and 180° and have a large uncertainty in comparison to the Cu–O(3) bond lengths, probably due to the proximity of the bond angles to 180° such that small uncertainties in the Cu–O(3) length causes large uncertainties in the bond angle. These bond angles are larger than the 164° to 165° for YBCO and

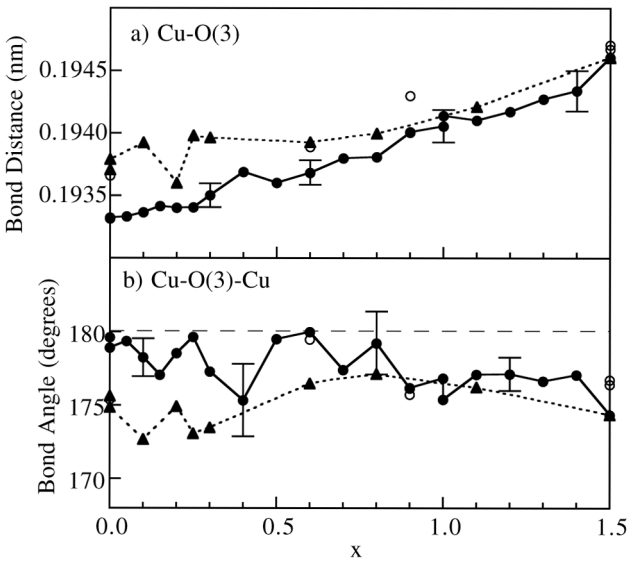

FIG. 6. The CuO_2 intraplanar Cu–O(3) bond lengths (a) and O(3)–Cu–O(3) bond angles (b) for the $(R_{1.5-x}Pr_xCe_{0.5})Sr_2Cu_2NbO_{10-\delta}$, R = Sm (▲), Eu (●), and deoxygenated R = Eu (○), series of compounds determined from refined atomic positions of the XRD data. Error bars show representative uncertainties in the refined bond lengths.

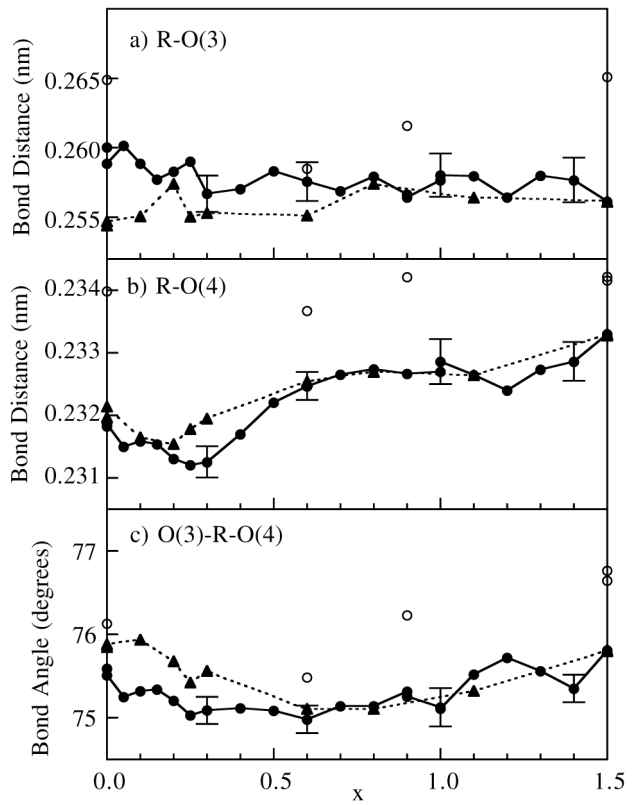

FIG. 7. The rare earth–nearest neighbor oxygen bond lengths and angles for the $(R_{1.5-x}Pr_xCe_{0.5})Sr_2Cu_2NbO_{10-\delta}$, R = Sm (▲), Eu (●), and deoxygenated R = Eu (○), series of compounds determined from refined atomic positions of the XRD data. Error bars show representative uncertainties in the refined bond lengths.

PrBCO (30) and closer to the 180° bond angle for Pr_2CuO_6 (31).

The local environment of the rare earth site in the $(R_{1.5}Ce_{0.5})$SCNO structure is also of interest since $(Pr_{1.5}Ce_{0.5})$SCNO falls into a subclass of high T_C cuprates which show anomalous Pr magnetism, a suppression of superconductivity associated with the Pr ion, and possible f-electron hybridization with the planar CuO_2 states (15, 16, 22). The rare earth site in this structure is eight-fold coordinated with the oxygen atoms in an adjacent CuO_2 plane, O(3), and the oxygen atoms in the square-planar oxygen layer of the R_2O_2 fluorite substructure, O(4). The R–O(3) and R–O(4) bond distances and the O(3)–R–O(4) bond angle for the $(Eu_{1.5-x}Pr_xCe_{0.5})$SCNO and $(Sm_{1.5-x}Pr_xCe_{0.5})$SCNO series of compounds are shown in Fig. 7. The R–O(3) bond distances fall between 0.255 and 0.260 nm and appear featureless in terms of Pr doping levels. In contrast, the R–O(4) bond distances fall between 0.231 and 0.233 nm and show a dip centered at $x \approx 0.3$ for R = Eu and at $x \approx 0.2$ for R = Sm. These features appear to be coordinated with the contraction of the c lattice parameters (Fig. 5). R–O(4) initially decreases as Pr is doped into $(Eu_{1.5}Ce_{0.5})$SCNO. At $x \approx 0.3$ (0.2 for R = Sm) where the $c(x)$ curve changes slope (Fig. 5b), R–O(4) reaches a minimum and begins to increase until about $x \approx 0.6$. At $x \approx 0.6$, where $c(x)$ has a minimum, R–O(4) plateaus until it reaches its final value at $x = 1.5$. In addition, from Fig. 5, we see that the range of the contraction of the c lattice parameter is about 0.007 nm. The range of the contraction in the R–O(4) bond distances is about 0.001 nm and, given that there are four of these bond distances per unit cell, appears to represent a significant part of the c lattice contraction, which will be discussed below. The O(3)–R–O(4) bond angles fall between 75° and 76° and show a downward slope in the region $0 < x < 0.3$, presumably reflecting the contraction of the R–O(4) bond length in this region.

The local environment of the rare earth site in the $(R_{1.5}Ce_{0.5})$SCNO structure is nearly identical to that of the RCO structure (Fig. 1d), which does not show anomalous Pr effects (17). The rare earth site resides in a fluorite-like layer in both structures with a CuO_2 plane on one side and the square-planar oxygen layer of the fluorite layer on the other. Both of these layers provide the nearest neighboring oxygen atoms in an eight-fold coordination, with the rare earth–fluorite structure oxygen bond length slightly shorter than the rare earth–CuO_2 planar oxygen bond lengths. However, the CuO_2 planes of the $(R_{1.5}Ce_{0.5})$SCNO structure are buckled in a manner like that in the RBCO structure, such that the Cu–O(3)–Cu bond angles are slightly less than 180°. This is in contrast to the RCO structure where

the Cu–O–Cu bond angles are 180° (31). In addition, the R–O(3) bond distances for the $(Eu_{1.5-x}Pr_xCe_{0.5})$SCNO and $(Sm_{1.5-x}Pr_xCe_{0.5})$SCNO series of compounds (Fig. 7) are shorter than the corresponding bond distance of 0.2688 nm for PrCO (31). Likewise (although to a lesser degree) the R–O(4) bond distances are smaller than the corresponding 0.2335 nm bond distance for PrCO (31). The O(3)–R–O(4) bond angles of these materials are larger than the corresponding ~74.5° of PrCO (31). These results indicate that the rare earth–fluorite structure is more compact in the $(R_{1.5}Ce_{0.5})$SCNO structure than in the RCO structure.

The RBCO structure has a rare earth crystallographic environment similar to that of the $(R_{1.5}Ce_{0.5})$SCNO structure, and in contrast of PrCO does show anomalous Pr effects. Although the rare earth site in the RBCO compounds is eight-fold coordinated with its nearest neighbor oxygen atoms, the rare earth site resides in an tetragonal-planar structure rather than a fluorite trilayer. Furthermore, the nearest neighbor oxygen atoms reside in two enclosing CuO_2 planes, and the rare earth–nearest neighbor oxygen bond lengths are symmetric about the c-axis. The RBCO structure does, on the other hand, show a buckling of the CuO_2 planes like the $(R_{1.5}Ce_{0.5})$SCNO structure. Furthermore, and more crucial to our understanding of the magnetic and electronic properties of these materials (see discussion below), the rare earth–CuO_2 planar oxygen bond distances are 0.2465 and 0.2434 nm for orthorhombic PrBCO (30) which are smaller than the distances for the $(R_{1.5-x}Pr_xCe_{0.5})$SCNO compounds.

The data of Fig. 5 also show lattice parameters and V_{cell}'s for several deoxygenated samples.. The results show that the lattice expand upon deoxygenation and quantify our earlier observation of an associated lattice expansion. Furthermore, upon deoxygenation, the thermal parameters of the O(2) site in the SrO planes (Fig. 1a) increased dramatically from reasonable physical values to very large nonphysical values. Since atomic site occupancies were held fixed during our refinements, this result suggests that the oxygen removed from the lattice comes primarily from the SrO layers. This interpretation is based upon the tendency of the Rietveld method to compensate for reductions in XRD line intensity due to reduced site occupancy (when the occupancy fraction is not refined) by increasing the site's thermal parameters. Bond distances and angles for several deoxygenated $(Eu_{1.5-x}Pr_xCe_{0.5})$SCNO compounds are also shown in Fig. 5 and 6. In general, the bond lengths are larger for the deoxygenated samples, consistent with the observed expansion of the lattice associated with deoxygenation.

C. Thermogravimetric Analysis

TGA results in a forming gas atmosphere reveal that all the $(R_{1.5-x}Pr_xCe_{0.5})$SCNO samples undergo a mass loss between 300 and 600°C (Fig. 8). Subsequent XRD analysis indicates this mass loss is due to the reduction

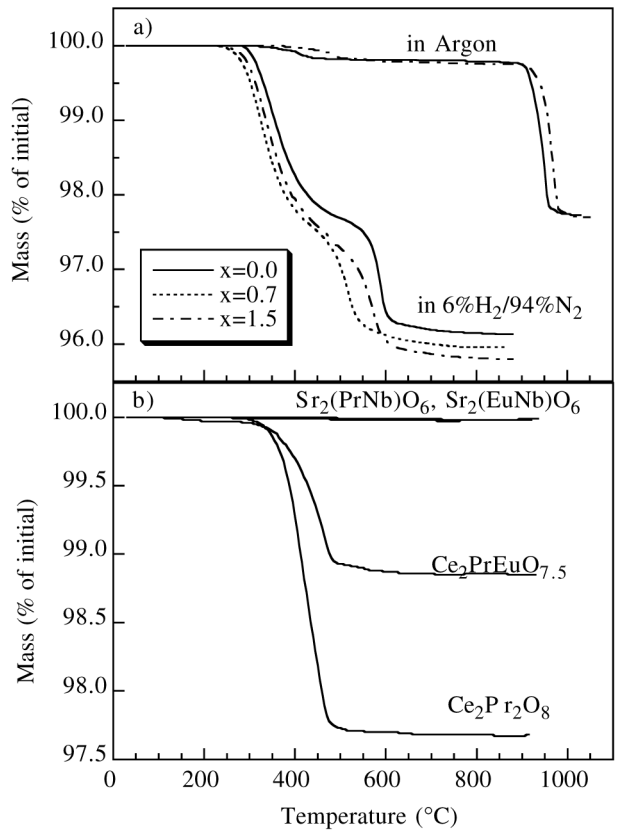

FIG. 8. (a) Representative TGA for the $(Eu_{1.5-x}Pr_xCe_{0.5})Sr_2Cu_2NbO_{10-\delta}$ series of compounds in argon and 6% H_2/94% N_2 atmospheres. (b) TGA results for Sr_2PrNbO_6, Sr_2EuNbO_6, $Ce_2PrEuO_{7.5}$, and $Ce_2Pr_2O_8$ in a 6% H_2/94% N_2 atmosphere.

$$(R'_{1.5}Ce_{0.5})Sr_2Cu_2NbO_{10-\delta} + H_{2\,(gas)} \rightarrow Sr_2R'NbO_6 + 0.25Ce_2R'_2O_{7-\xi} + 2Cu + (2.25 - \delta + 0.25\xi)H_2O_{(gas)}, \quad [1]$$

where R' is the solid solution of Pr with either Sm or Eu i.e., $R' = (R_{(1.5-x)/1.5}Pr_{x/1.5})$. The absolute oxygen stoichiometry of the $Sr_2R'NbO_6$ compounds was determined from careful measurements the change in mass during the synthesis of the $Sr_2(Eu_{1-z}Pr_z)NbO_6$ samples. TGA and HRROA performed over wide temperature and time ranges (up to 1000°C and 48 h) on the $Sr_2(Eu_{1-z}Pr_z)NbO_6$ samples in both forming gas and oxygen atmospheres showed no mass changes (see Fig. 8) for $z = 0.0$, 1.0 in forming gas). XRD indicated no structural or lattice parameter changes after these treatments, confirming that the stated oxygen stoichiometry for these compounds represents the equilibrium value under our TGA and HRROA methods.

The oxygen stoichiometry for the $Ce_2R'_2O_{7-\xi}$ compounds was determined from TGA and HRROA results for the $Ce_2(Eu_{2-y}Pr_y)O_{(7+y/2)}$ samples. The absolute oxygen stoichiometry of the $Ce_2(Eu_{2-y}Pr_y)O_{(7+y/2)}$ samples was determined through careful measurements of the change in mass during sample synthesis. TGA and HRROA of these samples in a forming gas atmosphere (with XRD analysis) indicated that they undergo a mass loss reduction of the form

$$Ce_2(Eu_{2-y}Pr_y)O_{(7+y/2)} + H_{2(gas)} \rightarrow Ce_2(Eu_{2-y}Pr_y)O_{(7-y)} + (y/2+\gamma)H_2O_{(gas)}, \quad [2]$$

between 350 and 450°C (Fig. 8). The mass loss results indicated that the change in oxygen stoichiometry scaled with Pr content and that $\gamma = 0.027(7) \times y$. Additional TGA and HRROA performed over wide temperature and time ranges (up to 1000°C and 48 h) on these samples confirmed that these values for γ represented the equilibrium oxygen stoichiometry of these compounds under the conditions of our TGA and HRROA and at least up to 1000°C. Therefore, ξ from Eq. [1] was determined as $\xi = \gamma = 0.027(7) \times [x(2.0/1.5)] = 0.036(9) \times x$.

For $Ce_2Eu_2O_7$, these results indicate that the Eu^{3+} ion stabilizes a Ce^{4+} ion in this compound such that the oxygen stoichiometry remains stable under the conditions of our TGA. This is in contrast to pure CeO_2 which, under the same TGA conditions, would be reduced to a oxygen deficient Ce oxide (7, 32). For the reduced $Ce_2Pr_2O_{7-\gamma}$, subsequent XRD revealed the same fluorite structure as $Ce_2Pr_2O_8$ but with the larger lattice parameter of 0.5402 nm which exactly matches that previously reported for $Ce_2Pr_2O_7$ (29). We also mention that recent magnetic (33) and electron energy loss spectroscopy (EELS) (34) results for $Ce_2Pr_2O_8$ and $Ce_2Pr_2O_{7-\gamma}$ indicate that Ce is in a 4+ valence state in both these compounds, and Pr is in a 4+ valence state in $Ce_2Pr_2O_8$ and a 3+valence state in $Ce_2Pr_2O_{7-\gamma}$. This result and the scaled change in oxygen stoichiometry in Eq. [2] suggest that a change in Pr valence accompanies the reduction reaction in Eq. [2].

Following the above analysis, δ was determined for the $(R_{1.5-x}Pr_xCe_{0.5})$SCNO and $(Pr_{1.5}Ce_{0.5})$SCTO compounds from the mass loss data of HRROA reduction of samples in forming gas at 900°C and from Eq. [1]. Figure 9 shows the results of values of δ in terms of both stoichiometric values and holes per Cu ion calculated (determined from a straightforward valence count; Pr^{3+} and Ce^{4+} valence states were assumed on the basis of recent EELS, specific heat, and magnetic measurements on the $(Eu_{1.5-x}Pr_xCe_{0.5})$SCNO series of compounds (15, 16, 22). Both systems show very little variation of δ indicating that oxygen stoichiometry and its contribution to carrier densities levels are relatively constant with Pr doping.

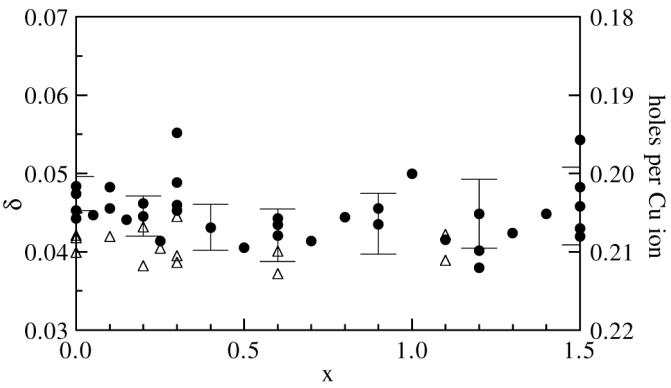

FIG. 9. δ's for the $(R_{1.5-x}Pr_xCe_{0.5})Sr_2Cu_2NbO_{10-\delta}$, R = Sm (△) and Eu (●), series of compounds determined from TGA in a 6% H_2/94% N_2 atmosphere. The right-hand y-axis provides a scale such that the δ's are expressed in terms of holes/Cu ion determined from a straightforward valence count. Error bars show representative uncertainties in the data due to the resolution of the measurement.

TGA and HRROA results for $(Pr_{1.5}Ce_{0.5})Sr_2Cu_2TaO_{10-\delta}$ and Sr_2PrNbO_6 showed a similar reduction chemistry as Eq. [1]. TGA results for the $(R_{1.5-x}Pr_xCe_{0.5})$SCNO, R = Sm, Eu, samples in air and oxygen show virtually no change in mass over the entire temperature range. However, small mass losses on the order of 0.007(3) formula unit oxygen could be detected with HRROA at 1050°C for 48 h; generally mass losses were small and varied widely.

TGA results for the $(R_{1.5-x}Pr_xCe_{0.5})$SCNO samples in argon indicate two regions of mass loss: the first between 350 and 500°C, and a larger mass loss between 900 and 1000°C (Fig. 8a). XRD of samples fired in argon at 750°C for 48 h show the $(R_{1.5-x}Pr_xCe_{0.5})$SCNO structure remained intact but that the lattice parameters had expanded (see Section IIIA). This indicates that the first mass loss at 350–500°C is due to a deoxygenation of the lattice and not a decomposition. Analysis of the mass loss in this region shows that δ's typically increase from ~0.045 to about 0.150. HRROA in forming gas of these deoxygenated samples corroborate the change in δ. Hence reduction in an argon atmosphere with 600°C < T < 900°C provides a reliable method for deoxygenating these compounds. Finally, XRD analyses of the samples fired in argon above the second mass loss point indicates that the mass loss is due to the decomposition:

$$(R'_{1.5}Ce_{0.5})Sr_2Cu_2NbO_{10-\delta} \rightarrow Sr_2R'NbO_6 + 0.25Ce_2R'_2O_{7-\zeta} + 2Cu_2O + (0.25-\delta+0.25\zeta)/2O_{2(gas)}, \quad [3]$$

where ζ was not determined.

IV. DISCUSSION

The contraction of the c lattice parameters and corresponding behavior of the V_{cell}'s for the $(R_{1.5-x}Pr_xCe_{0.5})$SCNO, R = Nd, Sm, Eu, series of compounds are unexpected given recent structural, magnetic, specific heat, and EELS measurements which independently indicate that the Pr ion is trivalent with a $^3H_4$ 4f ground state in these compounds (8, 15, 16, 22, 34). One might have expected that the V_{cell}'s of these compounds would scale with the mean ionic radii of the rare earth site in these compounds at a larger Pr^{3+} ion is doped in for the smaller Sm^{3+} and Eu^{3+} ion. However, the behavior of the V_{cell}'s is reminiscent of a mixed-valent Pr ion such that the average Pr ion radii is intermediate to that of the Pr^{3+} and the smaller Pr^{4+} ion and that variations in the Pr valence (and therefore the mean rare earth ionic radii) with Pr doping levels lead to the observed features in the c lattice parameters and the V_{cell}'s. Furthermore, the exact valence of the Pr ion in Pr-based high T_C cuprates has been a point of contention in the literature due to the anomalous suppression of superconductivity in PrBCO (17). Several proposed models for this suppression are based upon a band-filling mechanism driven by a mixed Pr ion (17, 35) or by strong interactions between the Pr 4f and CuO_2 planar O 2p states which manifest a mixed valent Pr ion (17, 35). However, our previous structural characterizations of the $(R_{1.5}Ce_{0.5})$SCNO, R = Nd, Sm, and Eu, compounds indicate that both the a and c lattice parameters scale with the rare earth ionic radii in this structure. If the contraction of the c lattice parameter were due to the presence of a smaller Pr^{4+} ion at the rare earth site, we would expect both the a and c lattice parameters to contract together. Therefore, we must conclude that a mixed valent Pr ion cannot account for the contraction of the c lattice parameter in these compounds.

The contraction of the c lattice parameter could also be caused by a mixed valent Ce ion or variations in oxygen stoichiometry since the XRD data indicate that the lattice parameters of these materials are dependent upon the oxygen stoichiometry (see Section IIIB). Previous magnetic and EELS measurements (8, 22, 34) indicate that the Ce ion is tetravalent in these materials. Furthermore, the discussion in the preceding paragraph on how the behavior of the contraction of the lattice is inconsistent with a mixed valent Pr ion is applicable to the Ce ion as well. TGA results indicate no significant variations in the oxygen stoichiometries of these compounds, and Fig. 9 shows no features in the δ's for these compounds which would be correlated to the behavior of the c lattice parameters. Hence, neither a mixed valent rare earth ion nor variations in oxygen stoichiometries can account for the c lattice parameter contractions.

Another possible explanation for the c lattice contraction arises from the observation that the features in the c lattice parameter and V_{cell}'s correspond to the electronic and magnetic transitions in the $(R_{1.5-x}Pr_xCe_{0.5})$SCNO phase diagrams. The $c(x)$ data for the $(Eu_{1.5-x}Pr_xCe_{0.5})$SCNO and $(Sm_{1.5-x}Pr_xCe_{0.5})$SCNO systems in Fig. 5 undergo a marked change of slope near x_{cr} for these systems (Fig. 2) and at $x \approx 0.6$, the onset of long-range Pr magnetic order. Likewise, $V_{cell}(x)$ shows a change of slope at $x \approx 0.3$ and 0.6. Furthermore, it is apparent that the R–O(4) bond lengths (Fig. 7b) play a significant role in the contraction of the c lattice parameter, and the R–O(4) bond lengths are likewise correlated with the electronic and magnetic transitions induced by the Pr ion in these compounds. These results indicate that the features in $c(x)$, $V_{cell}(x)$, and R–O(4)(x) are related to the unusual electronic and magnetic properties induced by the Pr ion in these materials and that the complex interactions responsible for these properties play a key role in the lattice dynamics of these compounds.

The nature of the relationship between the lattice dynamics and the interactions in these compounds is uncertain at this point. However, these compounds fall into a class of high T_C cuprates which show anomalous Pr magnetism and a suppression of superconductivity associated with the f-electronic states of the Pr or Cm ion (15–17, 22, 36). Although the mechanism for this suppression is not well understood, it is clear that hybridization between the f-electronic states and the neighboring O 2p electronic states play a key role in determining the electronic and magnetic properties of these high T_C cuprates (15–17, 22, 36). Indeed, the impact of f-electronic interactions on the electronic and structural properties of materials is well known (37). Hence, we suggest that the relationship between the lattice dynamics and the unusual electronic and magnetic properties of these compounds resides in the contributions of f-electronic interactions.

These analyses lead to the discussion of the R–O(3) bond lengths. Both $(Pr_{1.5}Ce_{0.5})$SCNO and $(Pr_{1.5}Ce_{0.5})$SCTO fall into a subclass of Pr-containing high T_C cuprates which show anomalously large Pr Néel temperatures (T_N) (15–17, 38–40). The anomalous T_N's indicate that the underlying Pr magnetic interactions in this category of cuprates are fundamentally different from those of rare earths in other high T_C cuprates. Analyses of the properties of these Pr-containing cuprates suggest that Pr magnetism is mediated through a superexchange interaction through the neighboring oxygen atoms and that there is significant interaction between the Pr 4f and neighboring oxygen 2p electronic states (15–17, 22, 27, 38–40). Furthermore, in those compounds which are doped and expected to be superconducting, namely $PrBa_2Cu_3O_7$, $(Pr_{1.5}Ce_{0.5})$SCNO, and $(Pr_{1.5}Ce_{0.5})$SCTO, the anomalous Pr magnetism and 4f-electronic interactions have been linked to the mechanism responsible for the suppression of superconductivity. For both superexchange and f-electronic interactions, the overlaps of the Pr 4f and CuO_2 planar O 2p electronic wave functions, and therefore the Pr–oxygen bond length, are

expected to be critical parameters of these interactions (15–17, 22, 27, 38–40)). For shorter bond lengths, greater Pr 4*f*–O 2*p* electronic wave function overlap occurs and the magnetic and *f*-electronic interactions should be stronger. For larger bond lengths, less overlap occurs and thus weaker interactions are expected. This relationship has been quantified for the $PrBa_2Cu_3O_6$, $TlBa_2PrCu_2O_7$, $TlSr_2PrCu_2O_7$, $HgSr_2PrCu_2O_6$, and $Pb_2Sr_2PrCu_3O_8$ compounds (40). The Pr T_N's for these compounds have been found to scale with the Pr–CuO_2 planar oxygen bond distance (Pr–O_{Cu}). For those Pr-containing cuprates which do not show anomalous Pr effects such as PrCO and $Bi_2Sr_2PrCu_3O_8$, the Pr–O_{Cu} bond distances are noticeably larger than for those compounds which show anomalous Pr magnetism (15–17 22, 27, 31, 39–41). Hence, the structural properties of these compounds are consistent with current understanding of anomalous Pr magnetism in high T_C cuprates.

Figure 10 illustrates the relationship between the Pr–O_{Cu} bond length and anomalous Pr magnetism in high T_C cuprates in terms of Pr T_N versus Pr–O_{Cu} bond lengths. The plot shows that for those compounds which show anomalous Pr magnetism the Pr–O_{Cu} bond lengths fall below ~0.256 nm, while those compounds which do not show anomalous Pr magnetism or other anomalous Pr effects the Pr–O_{Cu} bond lengths are above ~0.264 nm. The positions of both $(Pr_{1.5}Ce_{0.5})$SCNO and $(Pr_{1.5}Ce_{0.5})$SCTO on the plot indicate that both of these compounds belong to the subclass of high T_C cuprates which show anomalous Pr magnetism and a suppression of superconductivity. Finally, we point out that the oxygen atoms on the O(4) sites are also neighbors to the Pr sites in both $(Pr_{1.5}Ce_{0.5})$SCNO and $(Pr_{1.5}Ce_{0.5})$SCTO. While we expect the O(4) oxygen atoms to also play a role in these interactions, it is difficult to compare the *R*–O(4) bond lengths to these other Pr-containing cuprates since only $(Pr_{1.5}Ce_{0.5})$SCNO and $(Pr_{1.5}Ce_{0.5})$SCTO have a fluorite-type rare earth structure. All the other Pr compounds have a square- or tetragonal-planar rare earth layer and have no equivalent to the O(4) site.

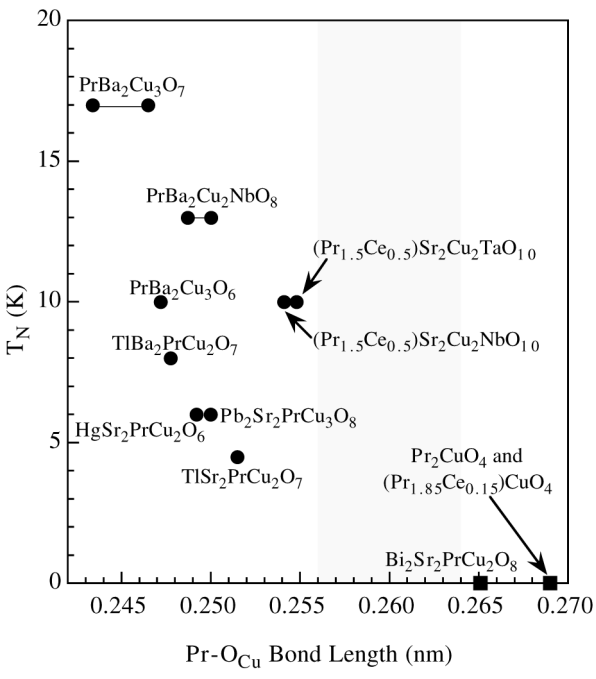

FIG. 10. T_N versus the Pr–CuO_2 planar oxygen bond length for Pr-containing cuprates. References for values are as follows: $PrBa_2Cu_3O_7$ and $PrBa_2Cu_3O_6$ (17, 30); $PrBa_2Cu_2NbO_8$ (27, 39); $TlBa_2PrCu_2O_7$, $TlSr_2PrCu_2O_7$, $HgSr_2PrCu_2O_6$, and $Pb_2Sr_2PrCu_3O_8$ (40); Pr_2CuO_4 (31); $Bi_2Sr_2PrCu_2O_8$ (15, 41); and $(Pr_{1.5}Ce_{0.5})Sr_2Cu_2TaO_{10-\delta}$ and $(Pr_{1.5}Ce_{0.5})Sr_2Cu_2TaO_{10-\delta}$ (this work, 15 16, 22).

Both $(Pr_{1.5}Ce_{0.5})$SCNO and $(Pr_{1.5}Ce_{0.5})$SCTO have been found to exhibit weak ferromagnetic (WF) behavior (14–16, 22) like that seen in some RCO cuprates such as Gd_2CuO_4, Y_2CuO_4, and Tb_2CuO_4 (42–44). The WF behavior has been attributed to a canting of the ordered Cu moments away from strictly antiferromagnetic (AF) alignment under the influence of asymmetric exchange interactions as discussed by Dzyaloshinsky and Moriya (45). Inherent in this proposed model for WF in these tetragonal compounds is an assumption that the Cu–O coordination is not square-planar due to local distortions of the crystal structure since in a strictly square-planar structure such asymmetric couplings should not exist (42–45). In the *R*CO compounds there is to date no clear evidence of such local structural distortions. Furthermore, the nature of these would-be distortions is unclear and a theoretical basis for the existence of WF in these compounds has yet to be established (42–44, 46). For $(Pr_{1.5}Ce_{0.5})$SCTO and the $(R_{1.5-x}Pr_xCe_{0.5})$SCNO, R = Nd, Sm, Eu, series of compounds, we were unable to address the issue of local distortions in the CuO_2 planes with our XRD data. Nevertheless, work in this area continues for the *R*CO, $(R_{1.5}Ce_{0.5})$SCNO, and $(R_{1.5}Ce_{0.5})$SCTO compounds in order to understand the microscopic origins of this WF (15, 16, 22, 42–44).

The TGA results on $(Pr_{1.5}Ce_{0.5})$SCTO and the $(R_{1.5-x}Pr_xCe_{0.5})$SCNO, R = Nd, Sm, Eu, series of compounds indicate that these materials are oxygen deficient with δ's of typically 0.045 with little variation (Table 1 and Fig. 9). A straightforward valence count based upon these δ's and Pr^{3+} and Ce^{4+} valence ions (15, 16, 22, 34) yield a carrier concentration of 0.20 to 0.21 holes per Cu ion (Fig. 9) for all of these compounds, indicating that the itinerant carrier concentration for superconducting $(Eu_{1.5}Ce_{0.5})$SCNO and $(Sm_{1.5}Ce_{0.5})$SCNO are the same for insulating $(Pr_{1.5}Ce_{0.5})$SCNO and $(Pr_{1.5}Ce_{0.5})$SCTO. This value of carrier concentration is qualitatively sufficient for superconductivity to occur in high T_C cuprates, especially considering the inherent inhomogeneity in oxygen stoichiometry and both Pr and Ce doping in the $(R_{1.5-x}Pr_xCe_{0.5})$SCNO materials.

Therefore, we should expect all these $(R_{1.5-x}Pr_xCe_{0.5})$SCNO compounds to be metallic and superconducting. This is in conflict with the observed metal-to-insulator transition induced by the Pr ion in these compounds and the strong insulating properties of both $(Pr_{1.5}Ce_{0.5})$SCNO and $(Pr_{1.5}Ce_{0.5})$SCTO (Fig. 2) (15, 16, 22). Hence, a straightforward valence count and a simple band-filling model cannot account for the insulating state induced by the Pr ion in these compounds. This result is similar to the situation for the $(R_{1-x}Pr_x)$BCO system where an insulating state induced by Pr is also in conflict with indications of a similar valence count. In the $(R_{1-x}Pr_x)$BCO system, the suppression of superconductivity is believed to involve carrier localization due to *f*-electronic interactions between the carrier states and the Pr 4*f* electronic states (17, 35, 47). Our results suggests that such a localization mechanism is a viable candidate to explain the suppression of superconductivity and insulating state induced by the Pr ion in the $(R_{1.5-x}Pr_xCe_{0.5})$SCNO compounds.

V. CONCLUSION

In conclusion, we have characterized $(Pr_{1.5}Ce_{0.5})$SCTO and $(R_{1.5-x}Pr_xCe_{0.5})$SCNO, R = Nd, Sm, and Eu, series of compounds with XRD, Rietveld refinement, and TGA. The XRD data show these compounds to be typically 98 fu% pure under the preparation conditions used. Rietveld refinements of the XRD data showed an unexpected contraction of the *c* lattice parameters for the $(R_{1.5-x}Pr_xCe_{0.5})$SCNO, R = Sm and Eu (and less definitively for R–Nd), series of compounds. The R–O(4) bond lengths appear to be a significant contributor to this contraction, and both the contraction and the R–O(4) bond lengths were found to be correlated with the unusual electronic and magnetic properties induced by the Pr ion in these compounds. These results suggest that these properties play a significant role in the lattice dynamics of these materials. This is in contrast to the related $(R_{1-x}Pr_x)$BCO materials where virtually no correlation between structural parameters and the analogous unusual properties induced by the Pr ion has been observed (17). Refined values for the R–O(3) bond lengths classify these compounds with other Pr containing high T_C cuprates which show anomalous Pr magnetism. This is in agreement with previous magnetic and specific heat measurements on these compounds (15, 16, 22) and is consistent with current understanding of anomalous Pr magnetism in high T_C cuprates (15–17, 22, 40). Unphysically large thermal parameters for the O(1) sites for all samples suggests that the rotation distortion of the NbO_6 octahedra reported for $(Nd_{1.5}Ce_{0.5})$SCNO is also present in all these materials. Finally, results for the deoxygenated compounds show that, upon deoxygenation of the lattice, the lattice expands and thermal parameters for the O(2) site increase dramatically from reasonable physical values to very large nonphysical values, suggesting that the oxygen is removed primarily from the SrO layers.

TGA results reveal a reliable technique for both determining the oxygen stoichiometries of these materials and deoxygenating these compounds. Results for the oxygen stoichiometries indicate that these materials are oxygen deficient with δ's near 0.045. A straightforward valence count indicate that a band-filling model cannot account for the suppression of superconductivity and insulating electronic state induced by the Pr ion in these compounds. Therefore, carrier localization and *f*-electronic interaction-based models proposed for the related $(R_{1-x}Pr_x)$BCO system remain viable candidates to explain the suppression of superconductivity and insulating state induced by the Pr ion in the $(R_{1.5-x}Pr_xCe_{0.5})$SCNO compounds (17, 47).

ACKNOWLEDGMENTS

The authors gratefully acknowledge support for this work from the National Science Foundation under Grant DMR-94-03895 and Lawrence Livermore National Laboratory under the auspices of the U.S. Department of Energy through Contract W-7405-ENG-48.

REFERENCES

1. J. G. Bednorz and K. A. Müller, *Z. Phys. B* **64,** 189 (1986).
2. M. K. Wu, J. R. Ashburn, C. J. Jorng, P. H. Hor, R. L. Meng, L. Gao, Z. J. Huang, Y. Q. Wang, and C. W. Chu, *Phys. Rev. Lett.* **58,** 908 (1987).
3. K. Yvon and M. Francois, *Z. Phys. B* **76,** 413 (1989).
4. "High Temperature Superconductivity" (J. W. Lynn, Ed.). Springer-Verlag, New York, 1990.
5. C. Park and R. L. Snyder, J. *Am. Ceram. Soc.* **78,** 3171 (1995).
6. (a) Li Rukang, Zhu Yingjie, Qian Yitai, and Chen Zuyao, *Physica C* **176,** 19 (1991); (b) Li Rukang, Zhu Yingjie, Xu Cheng, Chen Zuyao, Qian Yitai, and Fan Chengao, *J. Solid State Chem.* **94,** 206 (1991).
7. R. J. Cava, J. J. Krajewski, H. W. Zandbergen, R. B. Dover, W. F. Peck, Jr., and B. Hessen, *Physica C* **191**, 237 (1992).
8. T. J. Goodwin, H. B. Radousky, and R. N. Shelton, *Physic C* **204,** 212 (1992).
9. N. Brnicevis, I. Basic, P. Planicic, B. Grzeta, M. Tonkovic, M. Forsthuber, G. Hilscher, T. Holubar, H. Michor, H. Kirchmayr, and G. Schaudy, *Appl. Supercond.* **1,** 519 (1993).
10. N. Brnicevis, I. Basic, P. Planicic, M. Paljovic, M. Pozek, B. Ravkin, A. Dulcic, U. Desnica, D. Desnica, M. Reissner, W. Steiner, M. Forsthuber, G. Hilscher, and H. Kirchmayer, *in* "Electron Properties of High-T_C Superconductors" (H. Kuzmany, M. Mehring, and J. Fink, Eds.), Springer Series in Solid State Physics, Vol. 113. Springer-Verlag, Berlin, 1993.
11. G. Hilscher, T. Holubar, H. Michor, G. Schaudy, H. Kirchmayr, N. Brnicevis, I. Basic, P. Planicic, B. Grzeta, M. Vybornov, and P. Rogl, *Physica B* **194–196,** 2243 (1994).
12. Wang Shiwei, Qian Yitai, Li Rukang, Chen Zuyao, Wang Nanlin, Cao Liezhao, Zhou Guien, and Zhang Yuheng, *Physica C* **210,** 463 (1993).
13. (a) A. Ichinose, T. Wada, H. Yamauci, S. Tanaka, *J. Ceram. Soc. Jpn., Int. Ed.* **97,** 1053 (1989); (b) N. Murayama, E. Sudo, K. Kani, A. Tsuzuki, S. Kawakami, M. Awano, and Y. Torii, *Jpn. J. Appl. Phys.* **27,** L1623 (1988).
14. I. Felner, U. Yaron, U. Asaf, T. Kröner, and V. Breit, *Phys. Rev. B* **49,** 6903 (1994).

15. T. J. Goodwin, H. B. Radousky, R. N. Shelton, N. Rosov, and J. W. Lynn, *Phys. Rev. B* **55,** 3297 (1997).
16. T. J. Goodwin, Dissertation, University of California, Davis, 1995.
17. H. B. Radousky, *J. Mater. Res. Soc.* **7,** 1917 (1992). [See references therein]
18. S.-W. Cheong, J. D. Thompson, and Z. Fisk, *Phys. Rev. B* **39,** 4395 (1989).
19. S. B. Oseroff, D. Rao, F. Wright, D. C. Vier, S. Schultz, J. D. Thompson, Z. Fisk, S.-W. Cheong, M. F. Hundley, and M. Tovar, *Phys. Rev. B* **41,** 1934 (1990). [And references therein]
20. M. Tovar, X. Obradors, F. Pérez, S. B. Oseroff, R. J. Duro, J. Rivas, D. Chateigner, P. Bordet, and J. Chenavas, *Phys. Rev. B* **45,** 4729 (1992). [And referneces therein]
21. A. Rouco, X. Obradors, M. Tovar, F. Pérez, D. C. Hateigner, and P. Bordet, *Phys. Rev. B* **50,** 9024 (1994). [And references therein].
22. T. J. Goodwin, H. B. Radousky, and R. N. Shelton, *Phys. Rev. B* **56,** 5144 (1997).
23. A. C. Larson and R. B. Von Dreele, Los Alamos National Laboratory Report No. LAUR 86-748. [Unpublished]
24. H. Jhans, S. K. Malik, and R. Vijayaraghavan, *Physica C* **215,** 181 (1993).
25. (a) V. S. Filip'ev and E. G. Fesenko, *Sov. Phys.—Crystallogr.* **10,** 532 (1996); (b) M. F. Kupriyanov and V. S. Filip'ev, *Sov. Phys.—Crystallogr.* **8,** 278 (1963).
26. (a) H. W. Zandbergen, R. J. Cava, J. J. Krajewski, and W. F. Peck, Jr., *Physica C* **192,** 237 (1992); (b) H. W. Zandbergen, R. J. Cava, J. J. Krajewski, and W. F. Peck, Jr., *Physica C* **196,** 252 (1992).
27. M. Bennahmias, J. C. O'Brian, H. B. Radousky, T. J. Goodwin, P. Klavins, J. M. Link, C. A. Smith, and R. N. Shelton, *Phys. Rev. B* **46,** 11986 (1992).
28. M. Bruno and A. Mayer, *Ric. Sci.* **28,** 1168 (1958).
29. J. D. McCullough, *J. Am. Chem. Soc.* **72,** 1387 (1950).
30. C. K. Lowe-Ma and T. A. Vanderah, *Physica C* **201,** 233 (1992).
31. D. E. Cox, A. I. Goldman, M. A. Subramanian, J. Gopalakrishnan, and A. W. Sleight, *Phys. Rev. B* **40,** 6998 (1989).
32. D. J. M. Bevan and E. Summerville, Mixed Rare Earth Oxides, *in* "Handbook on the Physics and Chemistry of Rare Earths" (K. A. Gschneidner, Ed.), Vol. 3. North Holland, Amsterdam, 1991. [And references therein]
33. C. A. Smith, T. J. Goodwin, and R. N. Shelton, [In preparation]
34. S. C. Cheng, V. P. Dravid, T. J. Goodwin, R. N. Shelton, H. B. Radousky, *Phys. Rev. B* **53,** 11779 (1996).
35. D. Khomskii, *J. Superconductivity* **6,** 69 (1993). [And references therein]
36. (a) L. Soderholm, G. L. Goodman, U. Welp, C. W. Williams, and J. Bolender, *Physica C* **161,** 252 (1989); (b) L. Soderholm, G. L. Goodman, U. Welp, C. W. Williams, and J. Bolender, *J. Alloys Comp.* **181,** 13 (1992); (c) L. Soderholm, C.-K. Loong, *J. Alloys Comp.* **193,** 125 (1993).
37. (a) P. Wachter, Intermediate valence and heavy-fermion systems, *in* "Handbook on the Physics and Chemistry of Rare Earths" (K. A. Gschneidner, Ed.), Vol. 19. North Holland, Amsterdam, 1994; (b) M. Loewenhaupt and K. H. Fischer, Valence fluctuations and heavy-fermion 4*f* systems, *in* "Handbook on the Physics and Chemistry of Rare Earths" (K. A. Gschneidner, Ed.), Vol. 16. North Holland, Amsterdam, 1993; (c) H. Liu, Phenomenological approach to heavy-fermion systems, *in* "Handbook on the Physics and Chemistry of Rare Earths" (K. A. Gschneidner, Ed.) Vol. 17. North Holland, Amserdam, 1993.
38. A. Kebede, J. P. Rodriquez, I. Perez, T. Mihalisin, G. Myer, J. E. Crow, P. P. Wise, and P. Schlottmann, *J. Appl. Phys.* **69,** 5376 (1991).
39. N. Rosov, J. W. Lynn, H. B. Radousky, M. Bennahmias, T. J. Goodwin, P. Klavins, and R. N. Shelton, *Phys. Rev. B* **47,** 15256 (1993).
40. C. H. Chou, Y. Y. Hsu, J. H. Shieh, T. J. Lee, H. C. Ku, J. C. Ho, and D. H. Chen, *Phys. Rev. B* **53,** 6729 (1996). [And references therein]
41. Y. Gao, P. Pernambuco-Wise, J. E. Crow, J. O'Reilly, N. Spencer, H. Chen, and R. E. Salomon, *Phys. Rev. B* **45,** 7436 (1992).
42. S. B. Oseroff, D. Rao, F. Wright, D. C. Vier, S. Schultz, J. D. Thompson, Z. Fisk, S.-W. Cheong, M. F. Hundley, and M. Tovar, *Phys. Rev. B* **41,** 1934 (1990). [And references therein]
43. M. Tovar, X. Obradors, F. Pérez, S. B. Oseroff, R. J. Duro, J. Rivas, D. Chateigner, P. Bordet, and J. Chenavas, *Phys. Rev. B* **45,** 4729 (1992). [And references therin]
44. A. Rouco, X. Obradors, M. Tovar, F. Pérez, D. C. Hateigner, and P. Bordet, *Phys. Rev. B* **50,** 9024 (1994). [And references therein]
45. (a) I. Dzyaloshinsky, *J. Phys. Chem. Solids* **4,** 241 (1958); (b) T. Moriya, *Phys. Rev.* **120,** 91 (1960).
46. (a) D. Coffey, K. S. Bedell, and S. A. Trugman, *Phys. Rev. B.* **42**, 6509 (1990); (b) D. Coffey, T. M. Rice, and F. C. Zhang, *Phys. Rev. B* **44,** 10112 (1991). [And references therein]
47 R. Fehrenbacher and T. M. Rice, *Phys. Rev. Lett.* **70,** 3471 (1993).